Magnetic Field Spectral Evolution in the Inner Heliosphere

Nikos Sioulas, Zesen Huang, Chen Shi, Marco Velli, Anna Tenerani, Trevor A. Bowen, Stuart D. Bale, Jia Huang, Loukas Vlahos, L. D. Woodham, et al.

▶ **To cite this version:**

Nikos Sioulas, Zesen Huang, Chen Shi, Marco Velli, Anna Tenerani, et al.. Magnetic Field Spectral Evolution in the Inner Heliosphere. The Astrophysical journal letters, 2023, 943, 10.3847/2041-8213/acaeff . insu-04043844

HAL Id: insu-04043844
https://insu.hal.science/insu-04043844

Submitted on 24 Mar 2023

HAL is a multi-disciplinary open access archive for the deposit and dissemination of scientific research documents, whether they are published or not. The documents may come from teaching and research institutions in France or abroad, or from public or private research centers.

L'archive ouverte pluridisciplinaire **HAL**, est destinée au dépôt et à la diffusion de documents scientifiques de niveau recherche, publiés ou non, émanant des établissements d'enseignement et de recherche français ou étrangers, des laboratoires publics ou privés.

Distributed under a Creative Commons Attribution 4.0 International License

The Astrophysical Journal Letters, 943:L8 (7pp), 2023 January 20 https://doi.org/10.3847/2041-8213/acaeff
© 2023. The Author(s). Published by the American Astronomical Society.
OPEN ACCESS

Magnetic Field Spectral Evolution in the Inner Heliosphere

Nikos Sioulas[1], Zesen Huang (黄泽森)[1], Chen Shi (时辰)[1], Marco Velli[1], Anna Tenerani[2], Trevor A. Bowen[3], Stuart D. Bale[3,4], Jia Huang[5], Loukas Vlahos[6], L. D. Woodham[7], T. S. Horbury[8], Thierry Dudok de Wit[9], Davin Larson[3], Justin Kasper[5,10], Christopher J. Owen[11], Michael L. Stevens[12], Anthony Case[13], Marc Pulupa[3], David M. Malaspina[14,15], J. W. Bonnell[3], Roberto Livi[3], Keith Goetz[16], Peter R. Harvey[3], Robert J. MacDowall[17], Milan Maksimović[18], P. Louarn[19], and A. Fedorov[19]

[1] Department of Earth, Planetary, and Space Sciences, University of California, Los Angeles Los Angeles, CA 90095, USA; nsioulas@ucla.edu
[2] Department of Physics, The University of Texas at Austin, TX 78712, USA
[3] Space Sciences Laboratory, University of California, Berkeley, CA 94720-7450, USA
[4] Physics Department, University of California, Berkeley, CA 94720-7300, USA
[5] Climate and Space Sciences and Engineering, University of Michigan, Ann Arbor, MI 48109, USA
[6] Department of Physics, Aristotle University of Thessaloniki GR-52124 Thessaloniki, Greece
[7] Department of Physics, The Blackett Laboratory, Imperial College London, London, SW7 2AZ, UK
[8] The Blackett Laboratory, Imperial College London, London, UK
[9] LPC2E, CNRS and University of Orléans, Orléans, France
[10] BWX Technologies, Inc., Washington, DC 20002, USA
[11] Mullard Space Science Laboratory, University College London, Dorking, RH5 6NT, UK
[12] Harvard-Smithsonian Center for Astrophysics, Cambridge, MA 02138, USA
[13] Smithsonian Astrophysical Observatory, Cambridge, MA 02138, USA
[14] Astrophysical and Planetary Sciences Department, University of Colorado, Boulder, CO, USA
[15] Laboratory for Atmospheric and Space Physics, University of Colorado, Boulder, CO, USA
[16] School of Physics and Astronomy, University of Minnesota, Minneapolis, MN 55455, USA
[17] Solar System Exploration Division, NASA/Goddard Space Flight Center, Greenbelt, MD 20771, USA
[18] LESIA, Observatoire de Paris, Universit e PSL, CNRS, Sorbonne Universit e, Universit e de Paris, 5 place Jules Janssen, F-92195 Meudon, France
[19] IRAP, Université Toulouse III—Paul Sabatier, CNRS, CNES, Toulouse, France
Received 2022 November 6; revised 2022 December 28; accepted 2022 December 28; published 2023 January 24

Abstract

Parker Solar Probe and Solar Orbiter data are used to investigate the radial evolution of magnetic turbulence between $0.06 \lesssim R \lesssim 1$ au. The spectrum is studied as a function of scale, normalized to the ion inertial scale d_i. In the vicinity of the Sun, the inertial range is limited to a narrow range of scales and exhibits a power-law exponent of, $\alpha_B = -3/2$, independent of plasma parameters. The inertial range grows with distance, progressively extending to larger spatial scales, while steepening toward a $\alpha_B = -5/3$ scaling. It is observed that spectra for intervals with large magnetic energy excesses and low Alfvénic content steepen significantly with distance, in contrast to highly Alfvénic intervals that retain their near-Sun scaling. The occurrence of steeper spectra in slower wind streams may be attributed to the observed positive correlation between solar wind speed and Alfvénicity.

Unified Astronomy Thesaurus concepts: Solar wind (1534); Magnetohydrodynamics (1964); Interplanetary turbulence (830); Space plasmas (1544); Plasma astrophysics (1261)

1. Introduction

The solar wind flow transports a wide range of magnetic field and plasma fluctuations (Coleman 1968; Velli et al. 1989). Because fluctuations are predominantly Alfvénic (i.e., magnetic field and velocity fluctuations exhibit the correlations typical of outwardly propagating Alfvén waves; Bruno & Carbone 2013), and relative density fluctuations are very small, solar wind turbulence is usually discussed within the phenomenologies of incompressible magnetohydrodynamic (MHD).

During the expansion, nonlinear interactions result in a cascade of the energy toward smaller scales (Matthaeus & Velli 2011). Therefore, the energy injected into the solar wind at large scales, likely of solar origin, cascades downwards until it reaches ion scales, at which point the dynamics involve kinetic processes and structures such as ion cyclotron damping, kinetic Alfvén waves, kinetic scale current sheets, etc. (Leamon et al. 1999; Cranmer 2001; Dmitruk et al. 2004; Karimabadi et al. 2013; TenBarge & Howes 2013). Turbulence is thought to be one of the main processes contributing to the nonadiabatic expansion, as well as the acceleration of the solar wind (SW; Matthaeus & Velli 2011). MHD turbulence phenomenologies predict different power-law exponents depending on prevailing characteristics of turbulence, such as spatial wavenumber anisotropy (Goldreich & Sridhar 1995, 1997), intermittency (Mininni & Pouquet 2009; Chandran et al. 2015), and the scale-dependent correlation between velocity and magnetic field (Boldyrev 2006; Beresnyak & Lazarian 2010). The variability of solar wind turbulence properties in the inner heliosphere reflects the diversity of solar coronal sources, which modulate the density, velocity, temperature, and ion composition of the plasma. As a result, several factors, including the role played by large-scale gradients (Velli et al. 1989; Chandran & Perez 2019); the proximity to the heliospheric current sheet (HCS; Chen et al. 2021; Shi et al. 2022b); the presence of magnetic field switchbacks (Bourouaine et al. 2020; Martinović et al. 2021; Shi et al. 2022a); large-scale velocity shear in the SW (Coleman 1968), strongly influence the properties of turbulence, resulting in a wide range of spectral scalings. By means of fitting the power spectrum within a constant

Original content from this work may be used under the terms of the Creative Commons Attribution 4.0 licence. Any further distribution of this work must maintain attribution to the author(s) and the title of the work, journal citation and DOI.

range in the frequency domain, recent statistical studies of Parker Solar Probe (PSP) data, have recovered a nonevolving velocity spectral index close to $-3/2$, independent of the radial distance from the Sun (Shi et al. 2021), while the magnetic field spectrum steepens from a $-3/2$ slope at $\sim$0.2 au to a $-5/3$ slope at $\sim$0.6 au (Alberti et al. 2020; Chen et al. 2020; Shi et al. 2021).

Two scales are crucial to understanding the radial evolution of turbulence in the solar wind (1) the ion inertial scale $d_i = V_A/\Omega_i$, and (2) the thermal ion gyroradius, $\rho_i = V_{\mathrm{th},i}/\Omega_i$, where, $\Omega_i = e|B|/m_p$, is the proton gyrofrequency, e is the elementary charge, $|B|$ is the magnitude of the magnetic field, and m_p is the mass of the proton. With increasing heliocentric distance, both physical scales (d_i, ρ_i) increase (Duan et al. 2020; Cuesta et al. 2022).

It is thus natural to expect that the relative physical scale of fluctuations of a given frequency decreases as the solar wind expands. Here we aim to understand the radial evolution of magnetic turbulence and to study the basic features of scaling laws for solar wind fluctuations in terms of properly normalized physical scales. High resolution data from PSP (Fox et al. 2016), and Solar Orbiter (SO; Müller et al. 2020) covering heliocentric distances $13\,R_\odot \lesssim R \lesssim 220\,R_\odot$ are utilized and the radial evolution of the magnetic spectral index as a function of normalized wavenumber is investigated.

It is shown that closer to the Sun the magnetic field power spectrum exhibits a poorly developed inertial range that is characterized by a $-3/2$ spectral index. The inertial range extends to larger and larger scales as the solar wind expands into the interplanetary medium, with the inertial range spectral index steepening toward a $-5/3$ value. We demonstrate that the rate at which the steepening occurs is strongly dependent on magnetic energy excess and Alfvénicity of the fluctuations.

2. Radial Evolution of Magnetic Field Spectral Index

We considered overlapping intervals of duration $d = 24$ hr such that the beginnings of adjacent intervals are 8 hr apart. For each interval, the Fourier trace power spectral density $F(f_{\mathrm{sc}})$ was calculated, smoothed by averaging over a sliding window of a factor of 2, and transformed into a wavenumber spectrum expressed in physical units $E(\kappa^*)$ by virtue of the modified TH:

$$E(\kappa^*) = \frac{V_{\mathrm{tot}}}{2\pi \cdot \xi} F(f_{\mathrm{sc}})\ [nT^2 \cdot \xi], \tag{1}$$

where $\kappa^* = \kappa \cdot \xi = \frac{2\pi f_{\mathrm{sc}}}{V_{\mathrm{tot}}} \cdot \xi$, and, $\xi = d_i,\ \rho_{ci}$.

The radial evolution of the power spectrum as a function of spacecraft frequency and normalized by d_i is presented in Figures 1(a), (b) respectively. Due to the expansion of the solar wind but also in part because of the turbulent cascade, a decrease of $\sim$4 orders of magnitude in magnetic power is observed with increasing heliocentric distance.

The spectral index, α_B is obtained by taking a sliding window of one decade in the spacecraft-frame frequency (wavenumber) domain, over the smoothed spectra and calculating the best-fit linear gradient in log–log space over this window. For clarity, 10 radial bins have been used, and the median value of the spectral index as a function of frequency has been estimated for intervals that fall within the same bin. The color of the curve is keyed to the mean value of the distance R corresponding to the intervals within each bin. The results of this analysis are presented in Figure 2(a). In the inertial range, an energy cascade rate that is independent of

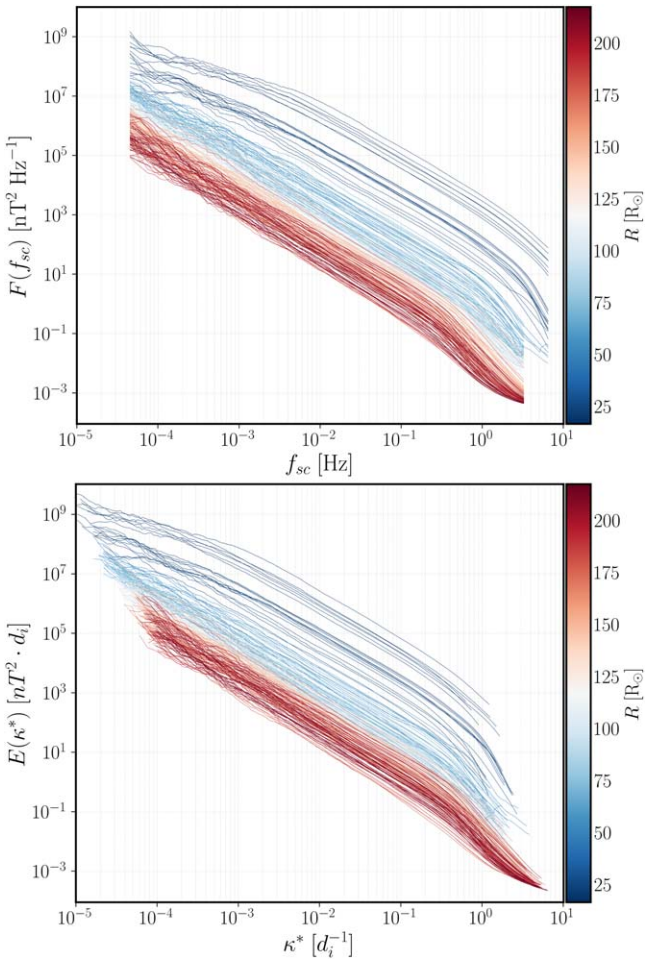

Figure 1. Magnetic field power spectrum, PSD at different heliocentric distances. The power spectrum is shown, as a function of (a) spacecraft frequency; (b) wavenumber $k^\circ = \ell^{-1}$ in units of d_i.

scale is expected, reflecting on the power spectrum in the form of a constant spectral index over this range of scales. In light of this, it can be seen that close to the Sun (dark blue line in Figure 2(a)), the inertial range is limited into a narrow range of frequencies (2×10^{-2}–2×10^{-1} Hz). As the solar wind expands in the interplanetary medium (1) a universal steepening (i.e., across all frequencies) is observed for the spectral index, α_B, at a constant f_{sc}; (2) the curves shift horizontally to lower and lower frequencies. As illustrated in Figure 2(a), the frequency range over which the spectral index is constant is migrating to the left while steepening with increasing distance, from $\alpha_B \approx -3/2$ to $\alpha_B \approx -5/3$. Similar behavior is observed at the largest scales. Closer to the Sun for $f_{\mathrm{sc}} \leqslant 2 \times 10^{-2}$ Hz, the spectrum gets progressively shallower at lower frequencies and obtains a value of $\alpha_B \approx -1$ at $f_{\mathrm{SC}} = 3 \times 10^{-4}$ Hz. As heliocentric distance increases, this low-frequency part of the spectrum gradually steepens, with all the frequencies approaching a $-5/3$ scaling. Therefore, as the solar wind propagates outward, the inertial range of the spectrum develops gradually, extending from higher frequencies to progressively lower and lower frequencies. Additionally, in accordance with Duan et al. (2020) the ion scale break, separating the inertial from the kinetic range is observed to migrate to lower frequencies with distance.

To cast the results in terms of relevant physical scales, we considered the evolution of α_B into the wavenumber domain

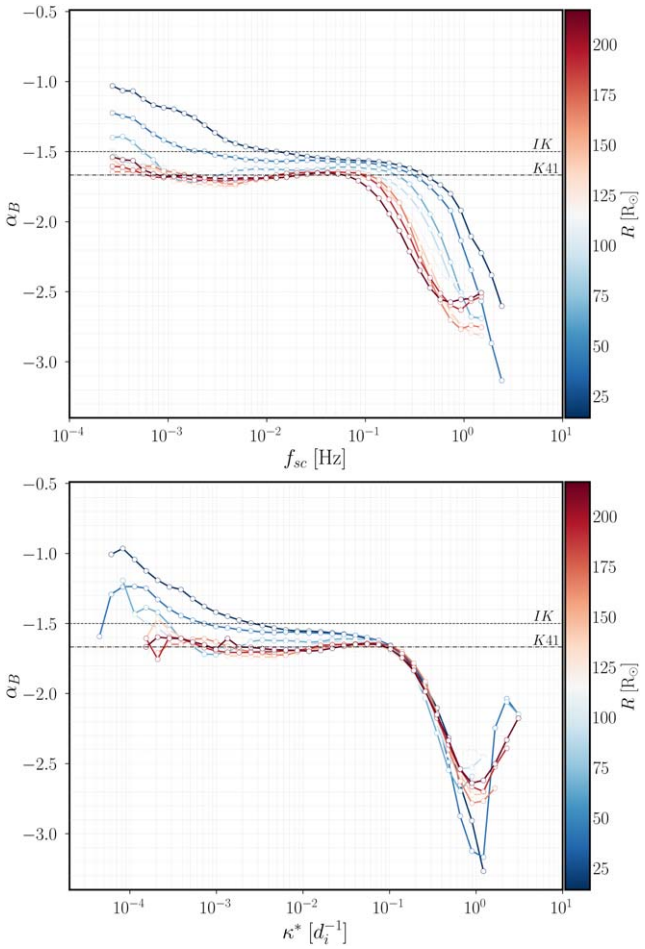

Figure 2. Evolution of magnetic field spectral index (α_B) as a function of distance, and (a) frequency in units of Hz (b) normalized wavenumber κ^* in units of d_i.

normalizing by either the ion inertial length (d_i) or the ion gyroradius (ρ_i).

The evolution of the spectral index as a function of distance (R) in the wavenumber domain normalized by d_i, is illustrated in Figure 2(b). It is readily seen that the vertical shifting of the curves to lower frequencies, observed in Figure 2(a), has vanished: all the curves roll over at $\kappa d_i \approx 0.1$ and overlap at smaller scales. The normalization does not appear to have a substantial impact on the radial development of the spectral index at large scales, $\kappa^* \lesssim 8 \times 10^{-2}$, since a steepening that closely resembles Figure 1(a) is obtained. On the other hand, as shown in Figure 1(b), the small scale break, demarcating the beginning of the transition region, $\kappa^* \approx 9 \times 10^{-2}$ (ρ_i^{-1}), does not show any remarkable evolution with distance and stays constant in physical space. We do not show plots using ρ_i as normalization because the spectra do not collapse as clearly into one curve at small scales, demonstrating that d_i is the more appropriate scale for such a normalization.

2.1. Dependence of α_B on Plasma Parameters

To disentangle the spectral variation with distance from changes due to the differing plasma parameters of different solar wind streams the dependence of α_B on the normalized cross-helicity σ_c

$$\sigma_c = \frac{E_o - E_i}{E_o + E_i}, \tag{2}$$

a measure of the relative amplitudes of inwardly and outwardly propagating Alfvén waves, and the normalized residual energy σ_r

$$\sigma_r = \frac{E_V - E_b}{E_V + E_b}, \tag{3}$$

indicating the balance between kinetic and magnetic energy is examined; $E_q = \frac{1}{2}\langle \delta \boldsymbol{q}^2 \rangle$ denotes the energy associated with the fluctuations of the field $\boldsymbol{q}$. In particular, $E_{o,i}$ can be estimated using Elsässer variables, defining outward and inward propagating Alfvénic fluctuations (Velli et al. 1991; Velli 1993)

$$\delta \boldsymbol{Z}_{o,i} = \delta \boldsymbol{V} \mp \mathrm{sign}(B_0^R)\delta \boldsymbol{b}, \tag{4}$$

$\delta \boldsymbol{B} = \boldsymbol{B} - \boldsymbol{B}_0$, $\boldsymbol{B}_0$ the background magnetic field, $\delta \boldsymbol{b} = \delta \boldsymbol{B}/\sqrt{\mu_0 m_p n_p}$ the magnetic fluctuations in Alfvén units, and B_0^r the ensemble average of B_R, are utilized to determine the polarity of the radial magnetic field (Shi et al. 2021). The variation of α_B with $V_{\rm sw}$, the ratio of magnetic to thermal pressure, $\beta \equiv n_p K_B T/(B^2/2\mu_0) \ll 1$, and the field/flow angle Θ_{BV} was also examined. Though we do not focus on β, and Θ_{BV} here, we will comment on these in Section 3. The evolution of α_B is investigated by fitting the magnetic spectrum over a constant range (10^{-3}–3×10^{-2} d_i^{-1}). To ensure that the plasma parameters under study do not vary significantly within the interval the duration of intervals has been reduced to $d = 1$ hr.

2.2. Solar Wind Speed, V_{SW}

As shown in Figure 4(a), within 30 R_s, no significant differences in spectral index with solar wind speed are found with an inertial range scaling, $\alpha_B \approx -3/2$. As the solar wind expands, the dependence on solar wind speed becomes more evident: steepening occurs regardless of solar wind speed, but it is more efficient for slower solar wind streams. As a result, at $R \approx 1$ au, the dependence of the spectral index on speed is clear, with the spectral index being consistent with a K41 scaling in the fast wind and a steeper scaling of ≈ -1.8 for the slowest winds. Categorizing the spectral index as a function of $\tau_{\rm adv}$, Figure 4(b), instead of radial distance one finds that for $\tau_{\rm adv} < 40$ hr no clear trend is observed for the spectral index as a function of wind speed. Beyond, this point, though steepening is monotonic with $\tau_{\rm adv}$ at all wind speeds. Overall, lower speed intervals display a significant radial steepening as compared to faster winds that only display a slight steepening. Closer to the Sun, however, there seems to be no dependence on wind speed on the spectral index, suggesting that the spectra are initially similar regardless of the wind speed.

2.3. Normalized Cross Helicity, σ_c, and Normalized Residual Energy σ_r

The joint $\sigma_c - \sigma_r$ distribution, estimated using 1 minute long moving averages of the respective time series is presented in Figure 3. The median and mean value of σ_c and σ_r for each bin are also shown as red and black crosses, respectively. The gray

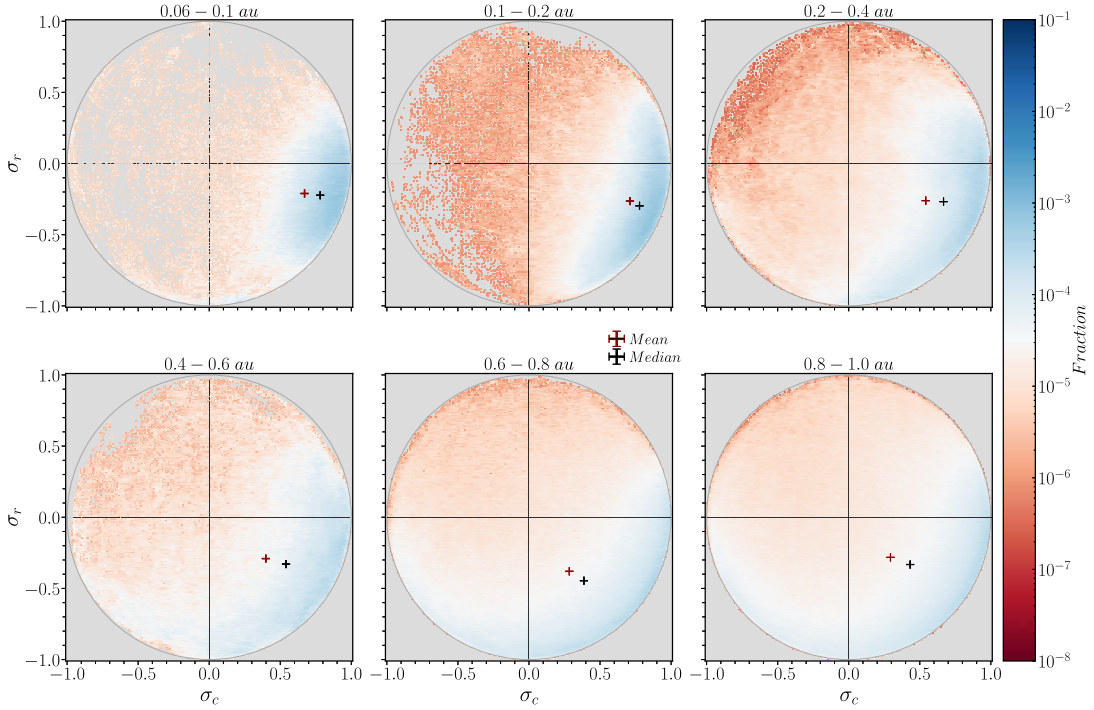

Figure 3. The joint distribution of normalized cross-helicity σ_c and normalized residual energy σ_r at different heliocentric distances.

circle defines fluctuations with perfect alignment between velocity and magnetic field, given by $\sigma_c^2 + \sigma_r^2 = 1$. Closer to the Sun (0.06–0.1 au) turbulence is highly Alfvénic, dominated by outwardly propagating waves ($\sigma_c \approx 0.85$), and in slight excess of magnetic energy ($\sigma_r \approx -0.15$). A small population of strongly magnetically dominated intervals characterized by very low Alfvénic content (i.e., $\sigma_r \approx -1$, and $\sigma_c \approx 0$), mostly associated with HCS crossings is also observed (see Shi et al. 2022b). At larger heliocentric distances the mean/median value of σ_c progressively decreases (Chen et al. 2020; Shi et al. 2021). Several mechanisms have been proposed to explain the diminishing dominance of outwardly propagating waves with increasing heliocentric distance due to wave reflection, including velocity shears (Bavassano et al. 1982) and the parametric decay instability (Tenerani & Velli 2013; Shoda et al. 2019). At 1 au, σ_r is clearly more negative than in the near-Sun environment, but it does not show a clear trend with radial distance. In the distance range of 0.6–1 au, most of the data points are concentrated in the lower half, with a few intervals having slightly positive σ_r values. In addition, data points located in the bottom left quadrant are increasing with distance, indicating a radially decreasing dominance of waves propagating outward.

The power-spectra of the fluctuating fields $\delta\boldsymbol{b}$, $\delta\boldsymbol{V}$, $\delta\boldsymbol{Z}_{o,i}$ have been obtained and both σ_c, and σ_r have been estimated by integrating the resulting spectra over a constant range (10^{-3}–$5 \times 10^{-2}\ d_i^{-1}$) in the wavenumber domain normalized by the ion inertial length. The dependence of the spectral index on $|\sigma_c|$ and σ_r as well as the radial distance (R) is presented in Figures 4(c), (d) for σ_c and σ_r, respectively. These show how highly Alfvénic ($|\sigma_c| \approx 1$) and energetically equipartitioned intervals display little spectral evolution, while evolution to significantly steeper spectra is associated with low $|\sigma_c|$ and/or large magnetic energy excess, with the data at large distances consistent with 1 au results (Podesta & Borovsky 2010; Chen et al. 2013; Bowen et al. 2018).

3. Conclusions

Using PSP and SO data from the inner heliosphere we have analyzed (1) how the statistical signatures of turbulence evolve with heliocentric distance and (2) the plasma parameters driving the evolution.

Identifying a plasma scale that grows radially at the same rate as the high frequency break point is crucial for this study in order to anchor the spectrum in normalized wavenumber space and enable meaningful comparison between intervals sampled at different heliocentric distances. Since the high frequency break point exhibits a power-law radial dependence with a scaling exponent 1.08 ± 0.03 (Duan et al. 2020; Lotz et al. 2022), then d_i, which grows radially as $\propto R^{1.04\pm0.01}$, provides a better normalization than ρ_i, which is characterized by a $\propto R^{1.48\pm0.02}$ radial scaling. It is important to emphasize that the goal here is not to find the quantity that has 1:1 correspondence with the high frequency break point. In fact, it is well known that intervals characterized by low ion β values exhibit a magnetic power spectral density that breaks at the ion inertial length (d_i), while high β intervals are characterized by a small scale break at the thermal ion gyroradius (ρ_i) (Chen et al. 2014). Thus, the pinning of the power spectrum at a constant κd_i scale, with increasing distance may be explained by the fact that plasma β values remain rather low in the inner heliosphere; see Figure 5. Another plasma scale that is correlated with the high frequency break point and should be considered by future investigations is the proton cyclotron resonance (Woodham et al. 2018).

Additionally, our analysis indicates that closer to the Sun, the inertial range of the magnetic field power spectrum is poorly developed i.e., the range of scales over which α_B remains constants is limited; its value is closer to $\alpha_B = -3/2$. As the solar wind expands into the interplanetary medium, the inertial range extends to progressively larger scales, while at

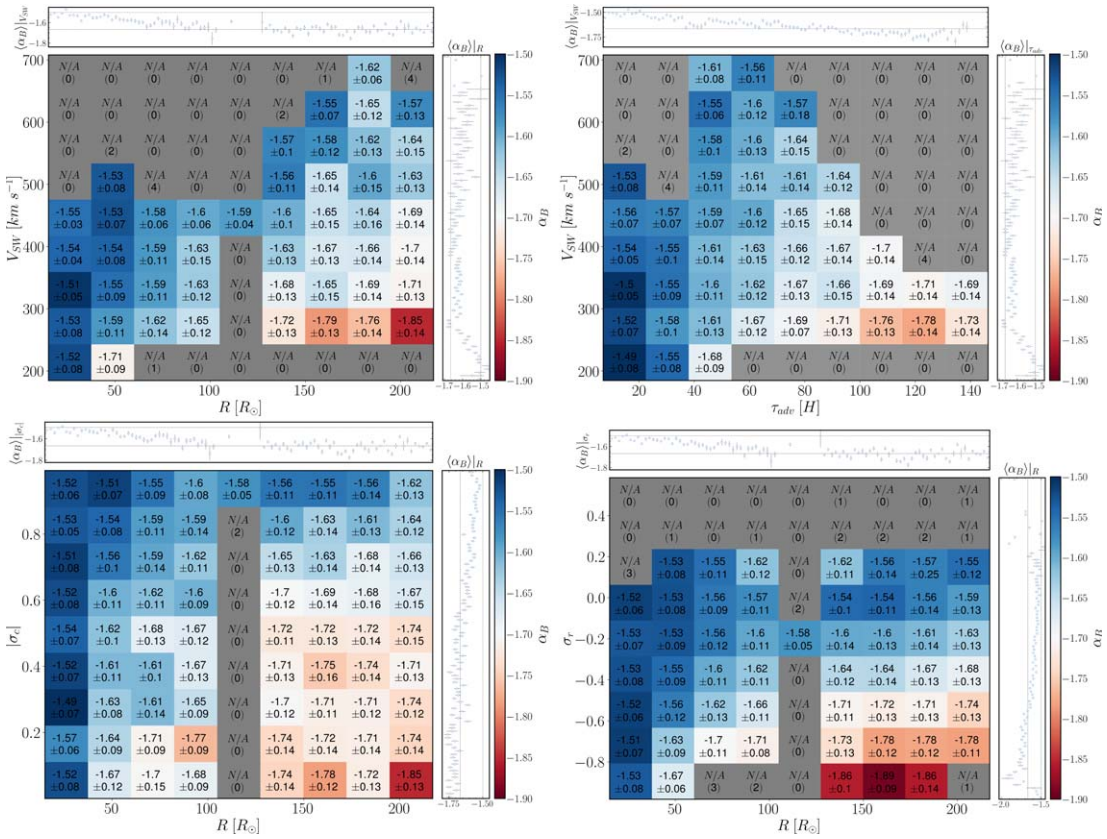

Figure 4. Magnetic field spectral index a_B as a function of $V_{\rm sw}$ and (a) heliocentric distance, (b) advection time $\tau_{\rm adv}$, as well as, a function of distance and (c) normalized cross helicity (σ_c), (d) normalized residual energy (σ_r).

the same time the inertial range spectral index steepens toward $\alpha_B = -5/3$.

We demonstrate that the rate at which α_B steepens is strongly dependent on the normalized residual energy and normalized cross helicity of the intervals under study. In particular, intervals with high Alfvénic content ($|\sigma_c| \approx 1$), and equipartitioned in $E_V - E_b$ ($\sigma_r \approx 0$) seem to retain their near-Sun scaling, and show a minor steepening with radial distance. In contrast, magnetically dominated and balanced intervals are observed to strongly steepen, resulting in anomalously steep inertial range slopes at 1 au, consistent with previous studies (Podesta & Borovsky 2010; Chen et al. 2013; Bowen et al. 2018).

While $|\sigma_c| \approx 1$ and $\sigma_r \approx 0$ values may be found in slow wind streams, especially closer to the Sun, they are statistically less relevant than in fast winds (Shi et al. 2021). As a result, the occurrence of steeper spectral indices in slower wind streams may be attributed to the observed positive correlation between solar wind speed and σ_c, σ_r.

Intervals with large magnetic energy excess closer to the Sun do not display the steep spectra observed at 1 au, attributed by Bowen et al. (2018) to the correlation between magnetic coherent structures and highly negative σ_r values (Mininni & Pouquet 2009). Recent studies (Cuesta et al. 2022; Sioulas et al. 2022), suggest that magnetic field intermittency is strengthened with increasing heliocentric distance in the inner heliosphere, but no similar analysis has been conducted for the velocity field. However, velocity spectra do not display radial evolution (Shi et al. 2021) and exhibit a scaling of $a_v = -3/2$ at 1 au (Chen et al. 2013). Based on our results, we expect that both the magnetic and velocity field spectra display a $-3/2$ scaling closer to the Sun, with the evolution of the magnetic spectrum related to the in situ generation of magnetic coherent structures during expansion. A study of the evolution of α_B and a_v as a function of radial distance as well as intermittency is ongoing. Turbulence in the solar wind is anisotropic with respect to the mean magnetic field (see, e.g., reviews by Schekochihin et al. 2009; Horbury et al. 2012; Oughton et al. 2015, and references therein). Horbury et al. (2008), Wicks et al. (2010), and Kiyani et al. (2012) have shown that when the field/flow angle Θ_{BV} is $\Theta_{BV} = 90°$, then the inertial range range scales like either $\alpha_B \approx -5/3$, or sometimes $\approx -3/2$, consistent with a critical balance cascade and dynamical alignment models respectively. In the parallel direction, $\Theta_{BV} = 0°$, it is nearer $\alpha_B \approx -2$. In contrast, when a global magnetic field is utilized to estimate θ_{BV}, no anisotropy in the spectral index as a function of Θ_{BV} is observed (Tessein et al. 2009; Chen et al. 2011). Though it is not shown here, we find no correlation between Θ_{BV} and α_B, using a global magnetic field. A similar result was obtained when considering the dependence of α_B on plasma β, suggesting that these two parameters are not related to the steepening of the spectrum. Further work to clarify the debate between a local, scale-dependent and global background magnetic field and its role on the spectral evolution is presented in a companion paper (Sioulas et al. 2023).

Our findings will help us gain a better understanding of how solar wind turbulence is generated and transported and will guide future models of solar wind turbulence.

This research was funded in part by the FIELDS experiment on the Parker Solar Probe spacecraft, designed and developed under NASA contract NNN06AA01C; the NASA Parker Solar Probe Observatory Scientist grant NNX15AF34G and the

HERMES DRIVE NASA Science Center grant No. 80NSSC20K0604. The instruments of PSP were designed and developed under NASA contract NNN06AA01C.

Appendix
Data Selection and Processing

We analyze magnetic field data from the Flux Gate Magnetometer (Bale et al. 2016), as well as plasma moment data from the Solar Probe Cup (SPC) and Solar Probe Analyzer (SPAN) part of the Solar Wind Electron, Alpha, and Proton suite between 2018 January 1, and 2022 June 15, encompassing the first 12 perihelia (E1–E12) of the PSP mission. SPC data have been utilized for E1-E8, while SPAN data for E9–E12. Quasi-thermal noise derived data (Moncuquet et al. 2020), have been preferred over SPAN or SPC data when available. Additionally, magnetic field and particle moment measurements from the Magnetometer instrument (Horbury et al. 2020), prioritizing burst data when available, and the Proton and Alpha Particle Sensor (SWA-PAS; Owen et al. 2020) on board the SO mission between 2018 June 1, to 2022 March 1, were considered. Following consideration of quality flags, time intervals that were found to be missing $\geqslant$1% and/or $\geqslant$10%, in the magnetic field and particle time series have been omitted from further analysis. The remaining intervals have been resampled linearly to the highest cadence possible, based on their initial resolution. Finally, in order to eliminate spurious spikes, a Hampel filter (Davies & Gather 1993) was applied to the plasma time series.

Converting the spacecraft-frame frequency derived PSD, $F(f_{sc})$ to a wavenumber PSD, $E(\kappa)$, far from the Sun is possible by means of Taylor's hypothesis (TH; Taylor 1938), $\kappa = 2\pi f_{sc}/V_{SW}$, which becomes questionable when both the Alfvén and spacecraft velocity are comparable to the velocity of the solar wind. Therefore, a modified version of TH that accounts for both wave propagation and spacecraft velocity is adopted (Klein et al. 2015): in the above expression for κ V_{sw} is replaced by $V_{tot} = |\boldsymbol{V}_{sw} + \boldsymbol{V}_a - \boldsymbol{V}_{sc}|$ where $\boldsymbol{V}_{sc}$ is the spacecraft velocity, where turbulence is assumed to be dominated by outwardly propagating Alfvén waves. Note that the TH remained either moderately or highly valid for the majority of time intervals examined, with only $\sim$1.53% of the intervals under study exhibiting $M_A < 1.5$, including a number sub-Alfvénic intervals during PSP $E_8 - E_{12}$ ($\sim$0.45% of the entire data set). Figure 5 illustrates the radial evolution of ion inertial length d_i, ion gyroradius ρ_i, and ion plasma β, quantities relevant to this study.

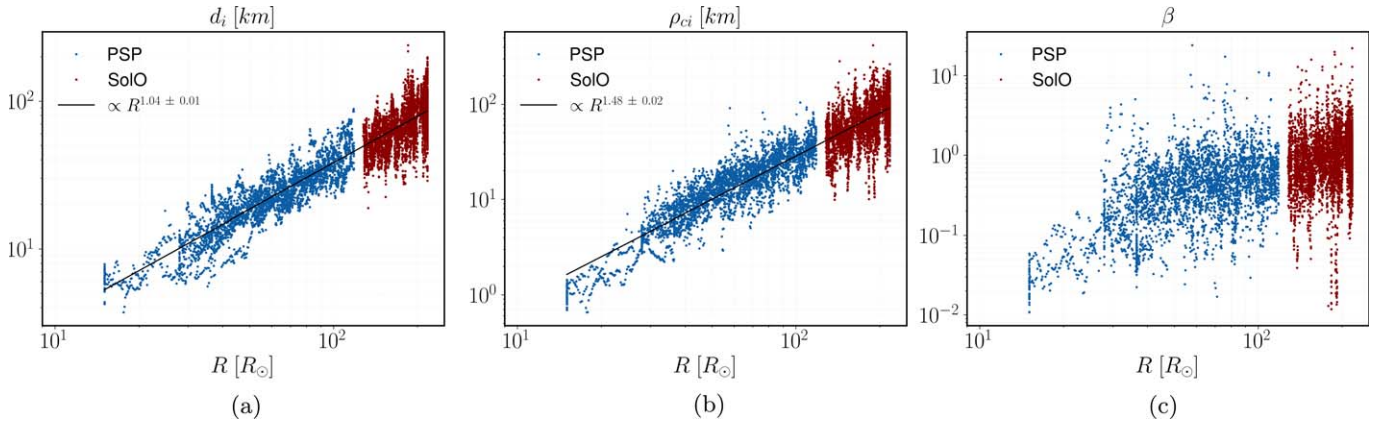

Figure 5. The radial evolution of (a) the ion inertial length d_i, (b) the ion gyroradius ρ_i, (c) ion plasma β.

ORCID iDs

Nikos Sioulas https://orcid.org/0000-0002-1128-9685
Zesen Huang (黄泽森) https://orcid.org/0000-0001-9570-5975
Chen Shi (时辰) https://orcid.org/0000-0002-2582-7085
Marco Velli https://orcid.org/0000-0002-2381-3106
Anna Tenerani https://orcid.org/0000-0003-2880-6084
Trevor A. Bowen https://orcid.org/0000-0002-4625-3332
Stuart D. Bale https://orcid.org/0000-0002-1989-3596
Jia Huang https://orcid.org/0000-0002-9954-4707
Loukas Vlahos https://orcid.org/0000-0002-8700-4172
L. D. Woodham https://orcid.org/0000-0003-2845-4250
T. S. Horbury https://orcid.org/0000-0002-7572-4690
Thierry Dudok de Wit https://orcid.org/0000-0002-4401-0943
Davin Larson https://orcid.org/0000-0001-5030-6030
Justin Kasper https://orcid.org/0000-0002-7077-930X
Christopher J. Owen https://orcid.org/0000-0002-5982-4667
Michael L. Stevens https://orcid.org/0000-0002-7728-0085
Anthony Case https://orcid.org/0000-0002-3520-4041
Marc Pulupa https://orcid.org/0000-0002-1573-7457
David M. Malaspina https://orcid.org/0000-0003-1191-1558
J. W. Bonnell https://orcid.org/0000-0002-0675-7907
Roberto Livi https://orcid.org/0000-0002-0396-0547
Keith Goetz https://orcid.org/0000-0003-0420-3633
Peter R. Harvey https://orcid.org/0000-0002-6938-0166
Robert J. MacDowall https://orcid.org/0000-0003-3112-4201
Milan Maksimović https://orcid.org/0000-0001-6172-5062
P. Louarn https://orcid.org/0000-0003-2783-0808
A. Fedorov https://orcid.org/0000-0002-9975-0148

References

Alberti, T., Laurenza, M., Milillo, A., et al. 2020, ApJ, 902, 84
Bale, S. D., Goetz, K., Harvey, P. R., et al. 2016, SSRv, 204, 49
Bavassano, B., Dobrowolny, M., Mariani, F., & Ness, N. F. 1982, JGR, 87, 3617
Beresnyak, A., & Lazarian, A. 2010, ApJL, 722, L110
Boldyrev, S. 2006, PhRvL, 96, 115002
Bourouaine, S., Perez, J. C., Klein, K. G., et al. 2020, ApJL, 904, L30
Bowen, T. A., Mallet, A., Bonnell, J. W., & Bale, S. D. 2018, ApJ, 865, 45
Bruno, R., & Carbone, V. 2013, LRSP, 10, 2
Chandran, B. D. G., & Perez, J. C. 2019, AGU Fall Meeting, 2019, SH51A–08
Chandran, B. D. G., Schekochihin, A. A., & Mallet, A. 2015, ApJ, 807, 39
Chen, C. H. K., Bale, S. D., Bonnell, J. W., et al. 2020, ApJS, 246, 53
Chen, C. H. K., Bale, S. D., Salem, C. S., & Maruca, B. A. 2013, ApJ, 770, 125
Chen, C. H. K., Chandran, B. D. G., Woodham, L. D., et al. 2021, A&A, 650, L3
Chen, C. H. K., Leung, L., Boldyrev, S., Maruca, B. A., & Bale, S. D. 2014, GeoRL, 41, 8081
Chen, C. H. K., Mallet, A., Yousef, T. A., Schekochihin, A. A., & Horbury, T. S. 2011, MNRAS, 415, 3219
Coleman, P. J. J. 1968, ApJ, 153, 371
Cranmer, S. R. 2001, in AIP Conf. Ser. 595, Radio Frequency Power in PLASMAS: 14th Topical Conf. (Melville, NY: AIP), 25
Cuesta, M. E., Parashar, T. N., Chhiber, R., & Matthaeus, W. H. 2022, ApJS, 259, 23
Davies, L., & Gather, U. 1993, J. Am. Stat. Assoc., 88, 782
Dmitruk, P., Matthaeus, W. H., & Seenu, N. 2004, ApJ, 617, 667
Duan, D., Bowen, T. A., Chen, C. H. K., et al. 2020, ApJS, 246, 55
Fox, N. J., Velli, M. C., Bale, S. D., et al. 2016, SSRv, 204, 7
Goldreich, P., & Sridhar, S. 1995, ApJ, 438, 763
Goldreich, P., & Sridhar, S. 1997, ApJ, 485, 680
Horbury, T. S., Forman, M., & Oughton, S. 2008, PhRvL, 101, 175005
Horbury, T. S., O'Brien, H., Carrasco Blazquez, I., et al. 2020, A&A, 642, A9
Horbury, T. S., Wicks, R. T., & Chen, C. H. K. 2012, SSRv, 172, 325
Karimabadi, H., Roytershteyn, V., Wan, M., et al. 2013, PhPl, 20, 012303
Kiyani, K. H., Chapman, S. C., Sahraoui, F., et al. 2012, ApJ, 763, 10
Klein, K. G., Perez, J. C., Verscharen, D., Mallet, A., & Chandran, B. D. G. 2015, ApJL, 801, L18
Leamon, R. J., Smith, C. W., Ness, N. F., & Wong, H. K. 1999, JGR, 104, 22331
Lotz, S., Nel, A. E., Wicks, R. T., et al. 2022, arXiv:2212.02441
Martinović, M. M., Klein, K. G., Huang, J., et al. 2021, ApJ, 912, 28
Matthaeus, W. H., & Velli, M. 2011, SSRv, 160, 145
Mininni, P. D., & Pouquet, A. 2009, PhRvE, 80, 025401
Moncuquet, M., Meyer-Vernet, N., Issautier, K., et al. 2020, ApJS, 246, 44
Müller, D., Cyr, O. C., St., Zouganelis, I., et al. 2020, A&A, 642, A1
Oughton, S., Matthaeus, W. H., Wan, M., & Osman, K. T. 2015, RSPTA, 373, 20140152
Owen, C. J., Bruno, R., Livi, S., et al. 2020, A&A, 642, A16
Podesta, J. J., & Borovsky, J. E. 2010, PhPl, 17, 112905
Schekochihin, A. A., Cowley, S. C., Dorland, W., et al. 2009, ApJS, 182, 310
Shi, C., Panasenco, O., Velli, M., et al. 2022a, ApJ, 934, 152
Shi, C., Velli, M., Panasenco, O., et al. 2021, A&A, 650, A21
Shi, C., Velli, M., Tenerani, A., Réville, V., & Rappazzo, F. 2022b, arXiv:2201.02894
Shoda, M., Suzuki, T. K., Asgari-Targhi, M., & Yokoyama, T. 2019, ApJL, 880, L2
Sioulas, N., Huang, Z., Velli, M., et al. 2022, ApJ, 934, 143
Sioula , N., Velli, M., Huang, Z., et al. 2023, ApJ, submitted (arXiv:2301.03896)
Taylor, G. I. 1938, RSPSA, 164, 476
TenBarge, J. M., & Howes, G. G. 2013, ApJL, 771, L27
Tenerani, A., & Velli, M. 2013, JGRA, 118, 7507
Tessein, J. A., Smith, C. W., MacBride, B. T., et al. 2009, ApJ, 692, 684
Velli, M. 1993, A&A, 270, 304
Velli, M., Grappin, R., & Mangeney, A. 1989, PhRvL, 63, 1807
Velli, M., Grappin, R., & Mangeney, A. 1991, GApFD, 62, 101
Wicks, R. T., Horbury, T. S., Chen, C. H. K., & Schekochihin, A. A. 2010, MNRAS, 407, L31
Woodham, L. D., Wicks, R. T., Verscharen, D., & Owen, C. J. 2018, ApJ, 856, 49